

## Supporting Information

### Enhanced electrocatalytic CO<sub>2</sub> reduction to methane via synergistic Sb and F dual-doping on copper foil under pulsed potential electrolysis

Kuan Wan,<sup>\*,a</sup> Xue Jiang,<sup>a</sup> Xin-Peng Li,<sup>a</sup> Zhe Cao,<sup>a</sup> Zhen-Hong He,<sup>a</sup> Weitao Wang,<sup>a</sup> Huan Wang,<sup>a</sup> Xiaojuan Lai,<sup>\*,a</sup> Zhao-Tie Liu<sup>\*,a,b</sup>

<sup>a</sup>Key Laboratory of Chemical Additives for China National Light Industry, College of Chemistry and Chemical Engineering, Shaanxi University of Science and Technology, Xi'an, 710021, China.

<sup>b</sup>School of Chemistry & Chemical Engineering, Shaanxi Normal University, Xi'an, 710119, China.

**Corresponding Author:** E-mail: wangkuan@sust.edu.cn (K. Wang); 3578466@163.com (X. Lai); ztliu@snnu.edu.cn (Z.-T. Liu).

## **Characterization.**

Transmission electron microscopy (TEM) images were obtained utilizing an FEI Talos F200x microscope operating at an accelerating voltage of 120 kV. High-resolution transmission electron microscopy (HR-TEM) and X-ray energy-dispersive spectroscopy (EDX) elemental mapping were conducted on the same FEI Talos F200x microscope at 200 kV. High-resolution HAADF-STEM images were obtained using a double spherical aberration (Cs) corrected FEI Talos F200x 60-300 microscope operating at 300 kV. The preparation of samples involved the deposition of a single drop of an ethanol solution containing nanoparticles onto carbon-coated molybdenum grids. X-ray diffraction (XRD) tests were performed using a SmartLab9KW instrument from Rigaku Corporation (Japan), which utilizes Cu K $\alpha$  radiation and is equipped with a detector of one-dimensional energy-dispersive. X-ray photoelectron spectroscopy (XPS) data were acquired using a K-Alpha scanning XPS microprobe (USA, Thermo Fisher Scientific). The samples for XPS were prepared by adhering small pieces of catalyst onto conductive adhesive. In-situ attenuated total reflectance Fourier-transform infrared spectroscopy (ATR-FTIR) tests were conducted through a Nicolet 6700 instrument (Thermo Fisher) equipped with a detector of mercury cadmium telluride (MCT). The electrolyte employed was a 0.5 M solution of CO<sub>2</sub>-saturated potassium bicarbonate (KHCO<sub>3</sub>), with a saturated Ag/AgCl reference electrode, and the cell configuration was an in-situ ATR-FTIR H-cell. It is important to note that all in-situ experimental conditions were meticulously aligned with those of pulsed electrolysis conditions, and spectra were recorded following four minutes of CO<sub>2</sub> electrolysis.

## Product analysis

The gaseous product underwent analysis utilizing a gas chromatograph (GC; Agilent 7890A), which was outfitted with a flame ionization detector (FID) for the detection of hydrocarbons and a thermal conductivity detector (TCD) for the measurement of hydrogen (H<sub>2</sub>) and carbon monoxide (CO). The quantification of the liquid product was performed using an NMR spectrometer (Bruker; AVANCE NEO 600 MHz) in DMSO-d<sub>6</sub>, with D<sub>2</sub>O serving as an internal standard. The FE of the gaseous products was determined using the following formula (1):

$$FE = \frac{nZF}{Q} \times 100\% \quad (1)$$

n represents the number of electrons involved in the electrode reaction, Z is the number of electrons transferred to generate a product, F denotes the Faraday constant, and Q is the quantity of electric charge.

In the presented equation, the variable n signifies the number of electrons participating in the electrode reaction, Z indicates the number of electrons transferred to yield a product, F represents the Faraday constant, and Q refers to the quantity of electric charge. The electrochemical active surface area (ECSA) was assessed based on the capacitive current recorded during double-layer charging (Cdl), which was analyzed in relation to the cyclic voltammetry (CV) scan rate. The potentials were established at 0.1 and 0.5 V vs RHE. The Cdl was calculated by plotting the difference in current densities ( $\Delta j = j_a - j_c$ ) at 0.2 V versus RHE in a 0.5 M KHCO<sub>3</sub> solution against the various scan rates, where  $j_a$  and  $j_c$  denote the anodic and cathodic current densities, respectively<sup>1</sup>. The scan rates employed in this investigation were 20, 40, 60, 80, 100, and 120 mV s<sup>-1</sup>.

## DFT calculations

First-principles calculations were conducted utilizing the Vienna Ab Initio Simulation Package (VASP)<sup>2, 3</sup>, which operates on the principles of density functional theory (DFT) and employs the projector augmented wave (PAW) method<sup>4</sup>. The Perdew-Burke-Ernzerhof (PBE) generalized gradient approximation (GGA-PBE) functional was utilized to characterize the exchange-correlation interactions<sup>5</sup>. Spin polarization calculations were incorporated into the analysis. A plane-wave basis cutoff energy of 450 eV was implemented. Structural optimization was performed using the conjugate gradient (CG) method, iterating until the total energy error fell below  $10^{-5}$  eV and the force on each atom was reduced to less than  $0.05 \text{ eV}/\text{\AA}^2$ . To mitigate periodic boundary effects, a vacuum layer of  $10 \text{ \AA}$  was introduced along the z-axis, with the lattice parameters defined as  $10.22 \text{ \AA} \times 10.22 \text{ \AA} \times 14.17 \text{ \AA}$ . The Brillouin zone was sampled using a  $3 \times 3 \times 1$  Monkhorst-Pack k-point grid.

### Calculation of Tafel slope and relative activation energy

In this study, the Arrhenius-like analysis method was used to study the influence of catalyst composition on the activation energy ( $E_a$ ). The traditional Arrhenius equation relies on temperature change, but this experiment indirectly evaluates the relative  $E_a$  level by comparing the exchange current density ( $j_0$ ) of different catalysts<sup>6,7</sup>. According to the Arrhenius equation (2):

$$j_0 = A e^{-E_a/RT} \quad (2)$$

Assuming that the difference of the preexponential factor (A) is small among different catalysts, the higher the exchange current density ( $j_0$ ), the lower the corresponding  $E_a$ <sup>8,9</sup>.

The linear sweep voltammetry (LSV) was used to measure the current density in the low overpotential region at normal temperature. The Tafel curve is drawn, and the Tafel slope and intercept are obtained by fitting. The calculation method of  $j_0$  is shown in formula 3

$$j_0 = 10^{\text{intercept}} \quad (3)$$

The relationship between different catalysts and activation energy is shown in formula 4:

$$\frac{E_{a,CuSbF-ED}}{E_{a,Contrast}} = \frac{\ln(j_{0,Contrast})}{\ln(j_{0,CuSbF-ED})} \quad (4)$$

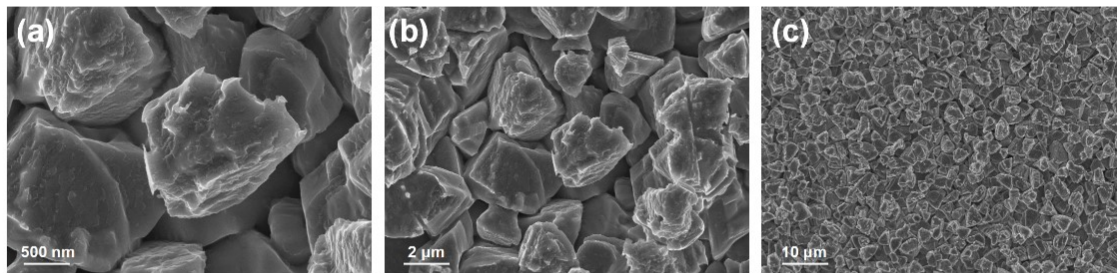


**Fig. S1.** The SEM images of (a-c) SEM images of the etched copper foil.

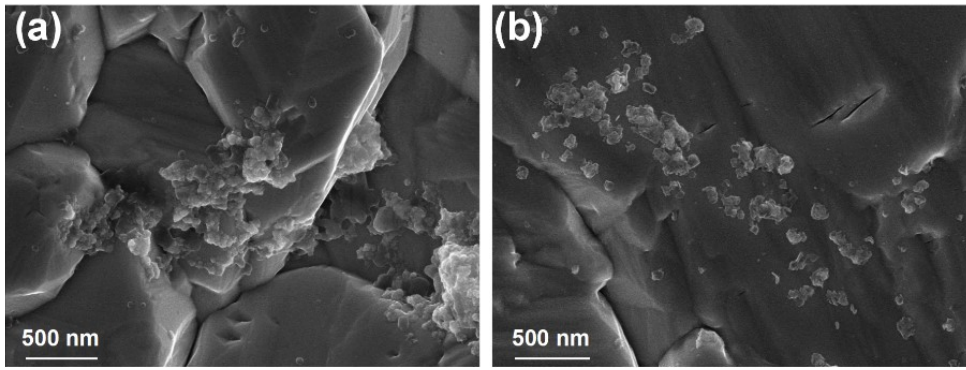


**Fig. S2.** The SEM images of (a,b) CuSbF-ED.

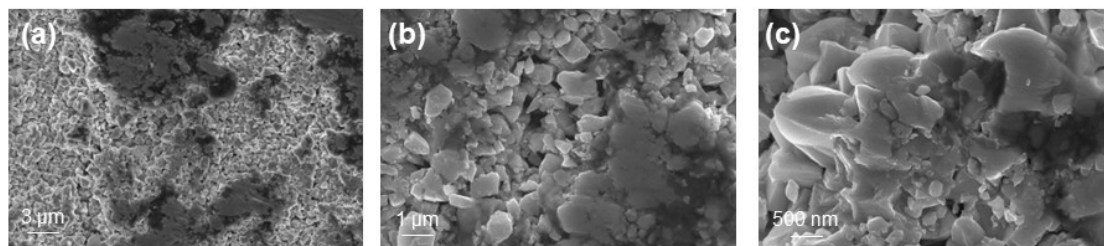


**Fig. S3.** The SEM images of (a-c) CuSb-ED.

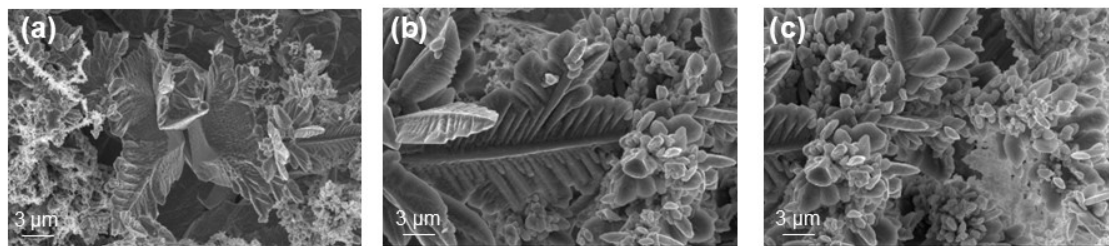


**Fig. S4.** The SEM images of (a-c) CuF-ED.

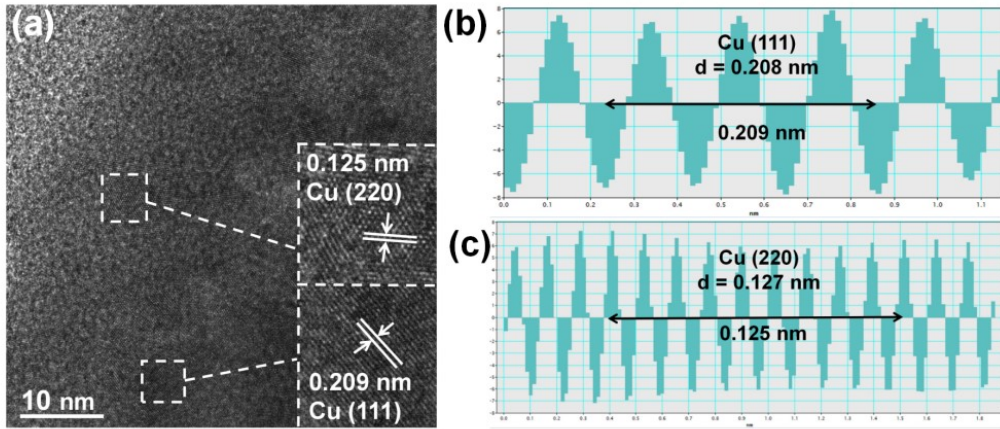


Fig. S5. The TEM image of CuSbF-ED.

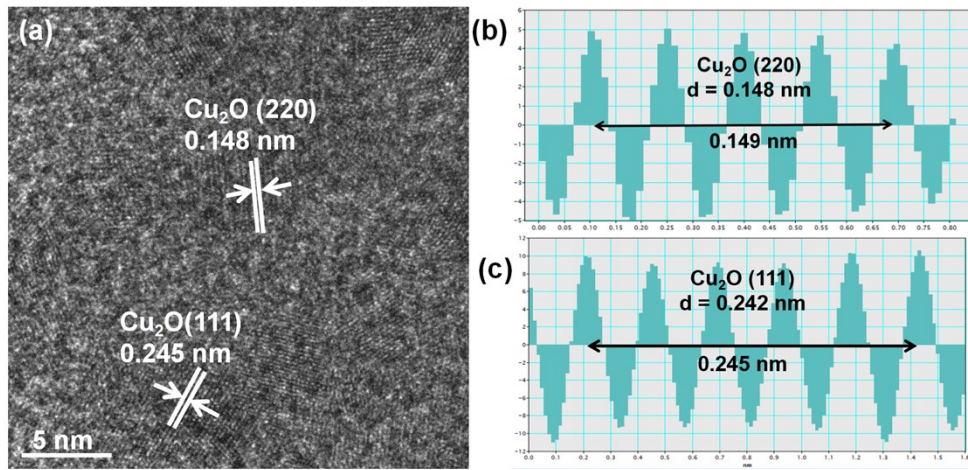
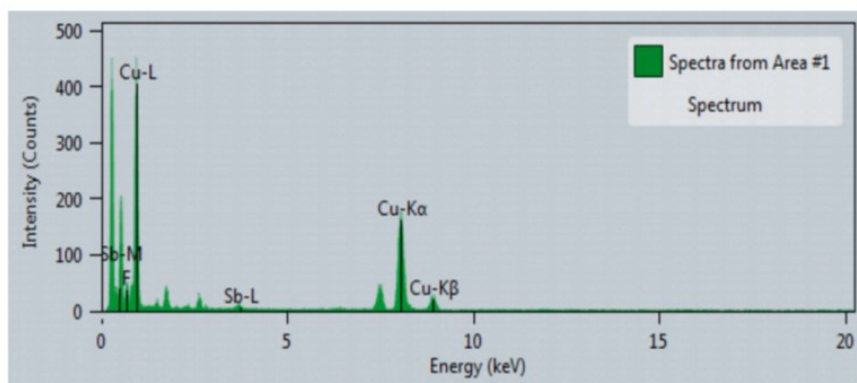


Fig. S6. The TEM image of CuSbF-ED.



Element	Line type	Mass fraction(%)
F	K	7.08
Cu	K	90.6
Sb	L	2.32
Total		100

**Fig. S7.** The TEM-EDS maps of F, Cu and Sb for CuSbF-ED.

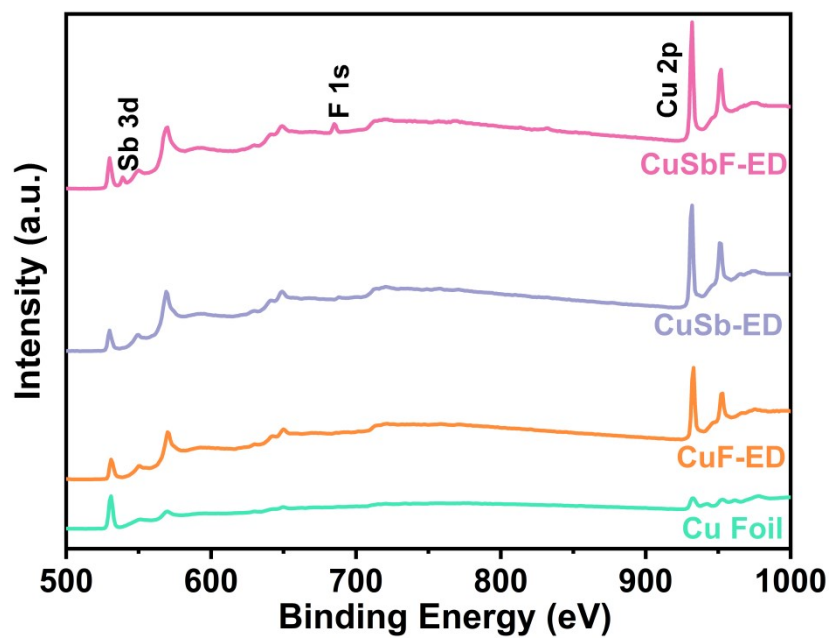
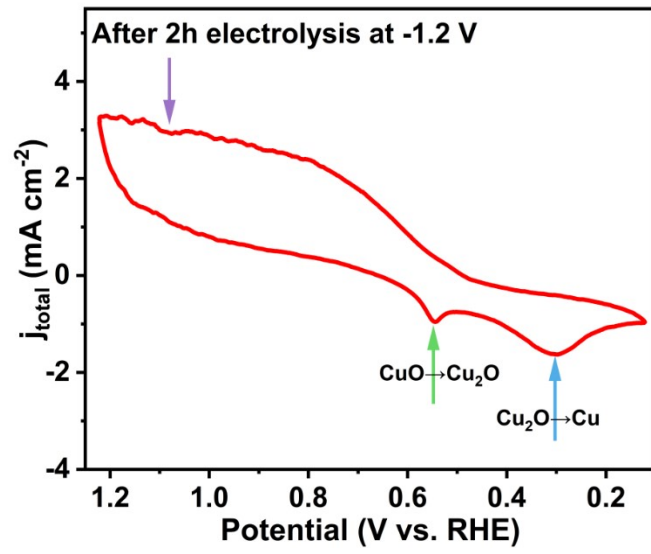
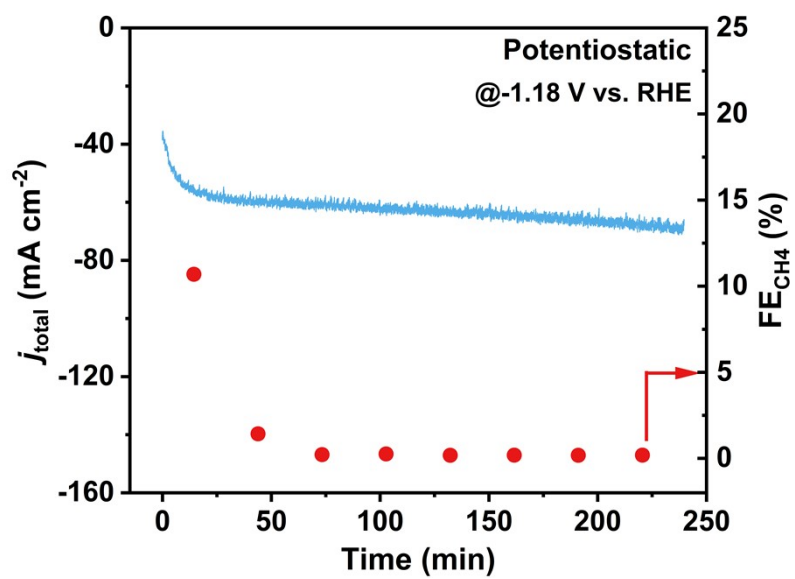


Fig. S8. The full XPS spectra of Cu foil, CuF-ED, CuSb-ED, and CuSbF-ED.



**Fig. S9.** CV curve of CuSbF-ED after 2 h electrolysis at -1.2 V in  $\text{CO}_2$ -saturated 0.5 M  $\text{KHCO}_3$ .



**Fig. S10.** Stability test using the potentiostatic method ( $E_c = -1.2$  V vs RHE).

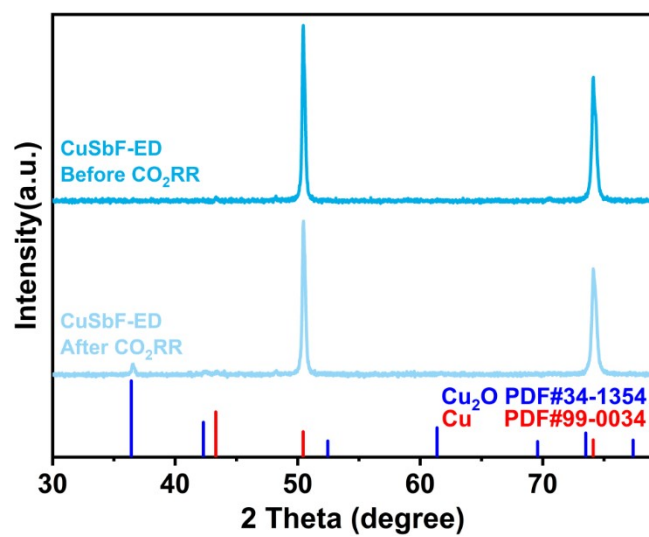


**Fig. S11.** XRD spectra of CuSbF-ED catalyst before and after pulse electrolytic reaction in CO<sub>2</sub>-saturated 0.5 M KHCO<sub>3</sub> solution.

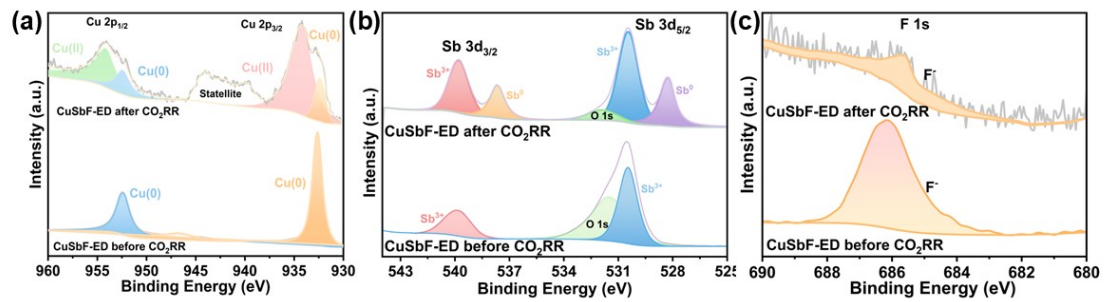


**Fig. S12.** XPS spectra of CuSbF-ED catalyst before and after pulse electrolytic reaction in CO<sub>2</sub>-saturated 0.5 M KHCO<sub>3</sub> solution. (a) Cu 2p, (b) Sb 3d, and (c) F 1s.

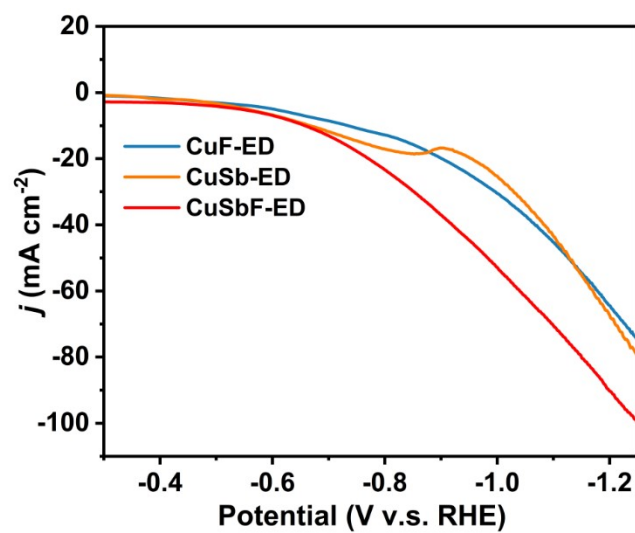


**Fig. S13.** Linear sweep voltammetry curves of CuF-ED, CuSb-ED, and CuSbF-ED in  $\text{CO}_2$ -saturated 0.5 M  $\text{KHCO}_3$  solution.

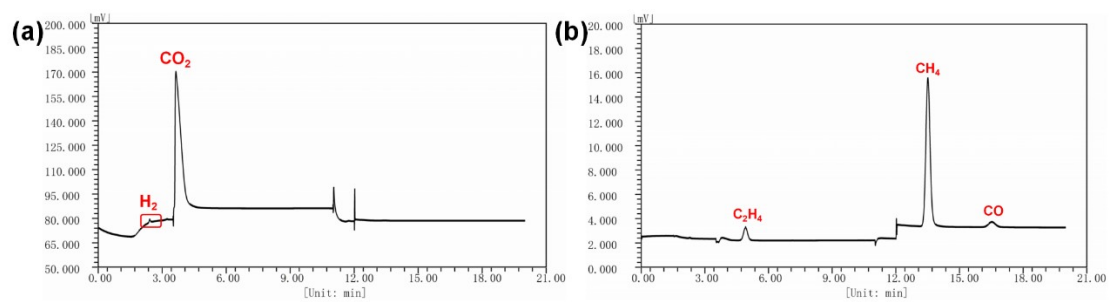


**Fig. S14.** A representative set of chromatographs during the analysis of one aliquot of the sample gas, which was produced on CuSbF-ED catalyst at 1.2 V vs. RHE.

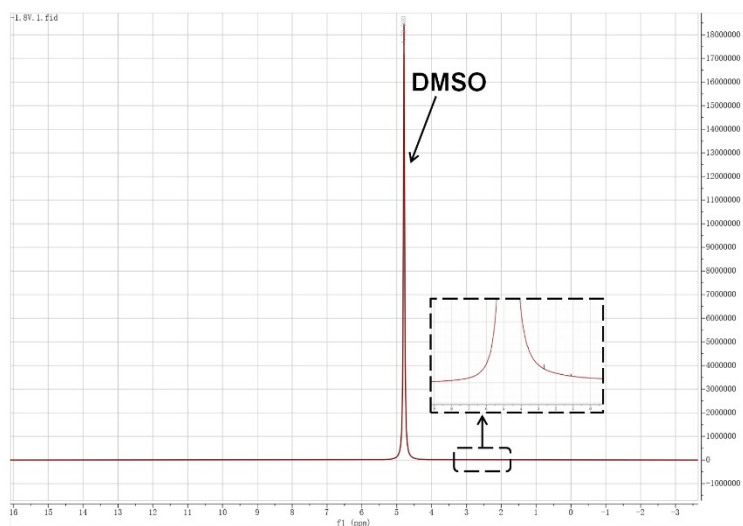


**Fig. S15.** Representative NMR spectrum taken on the liquid products.

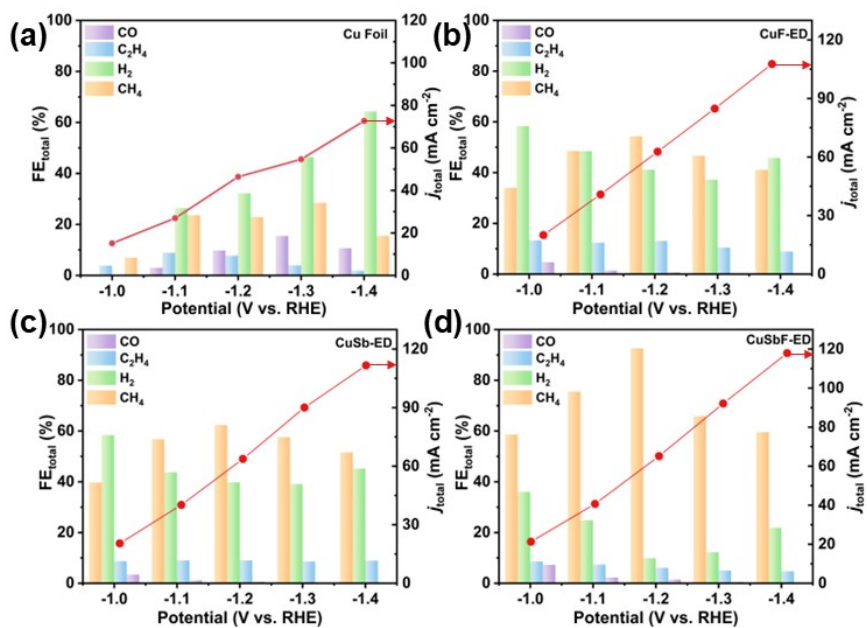


**Fig. S16.** The FE<sub>total</sub> of (a)Cu Foil, (b) CuF-ED, (c) CuSb-ED, and (d) CuSbF-ED in CO<sub>2</sub>-saturated 0.5 M KHCO<sub>3</sub> solution.

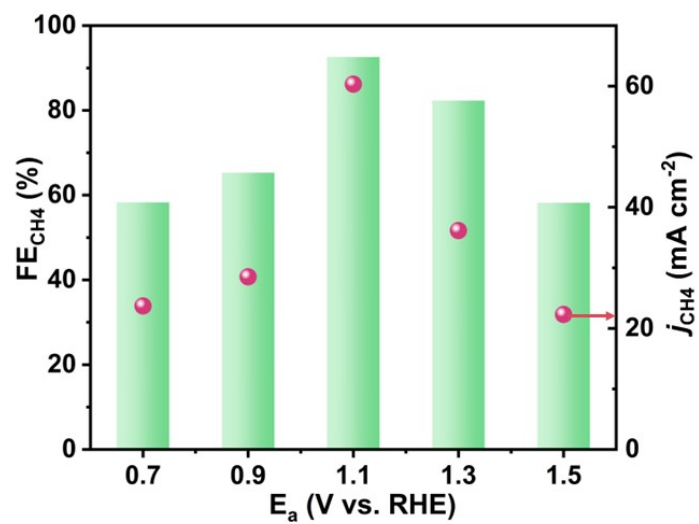


**Fig. S17.**  $FE_{CH_4}$  and  $j_{CH_4}$  of CuSbF-ED at different anode voltages.

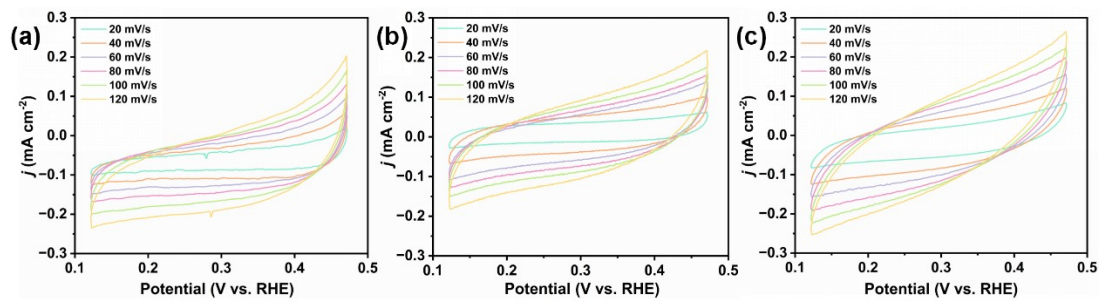


**Fig. S18.** Cyclic voltammograms with different scan rate of (a) CuF-ED, (b) CuSb-ED, and (c) CuSbF-ED.

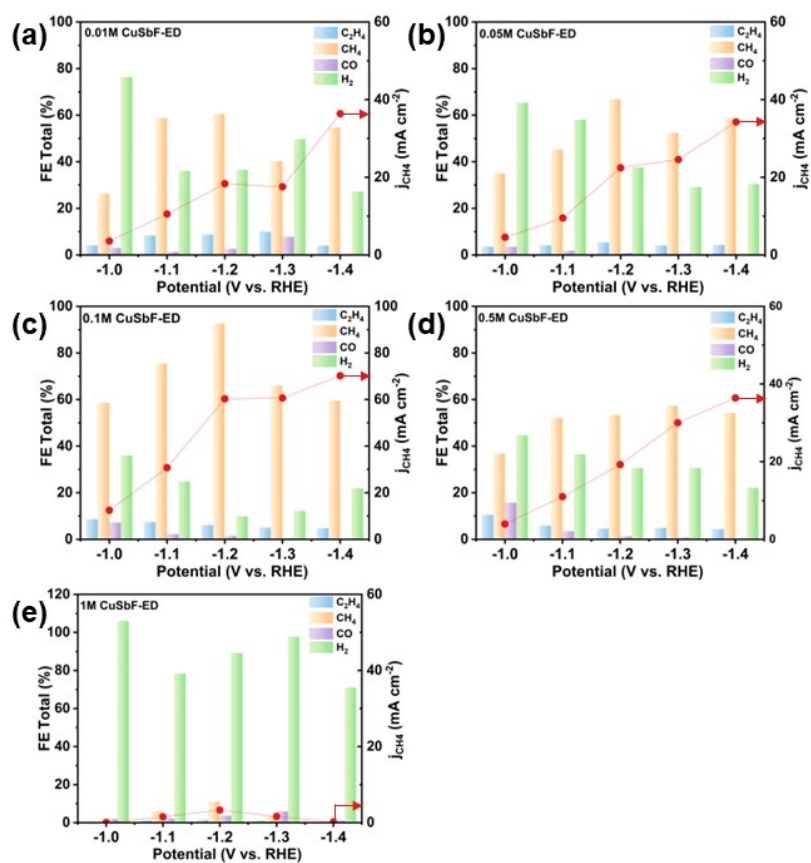


**Fig. S19.** The FE<sub>Total</sub> of (a) 0.01 M CuSbF-ED, (b) 0.05 M CuSbF-ED, (c) 0.1 M CuSbF-ED, (d) 0.5 M CuSbF-ED, and (e) 1 M CuSbF-ED in CO<sub>2</sub>-saturated 0.5 M KHCO<sub>3</sub> solution.

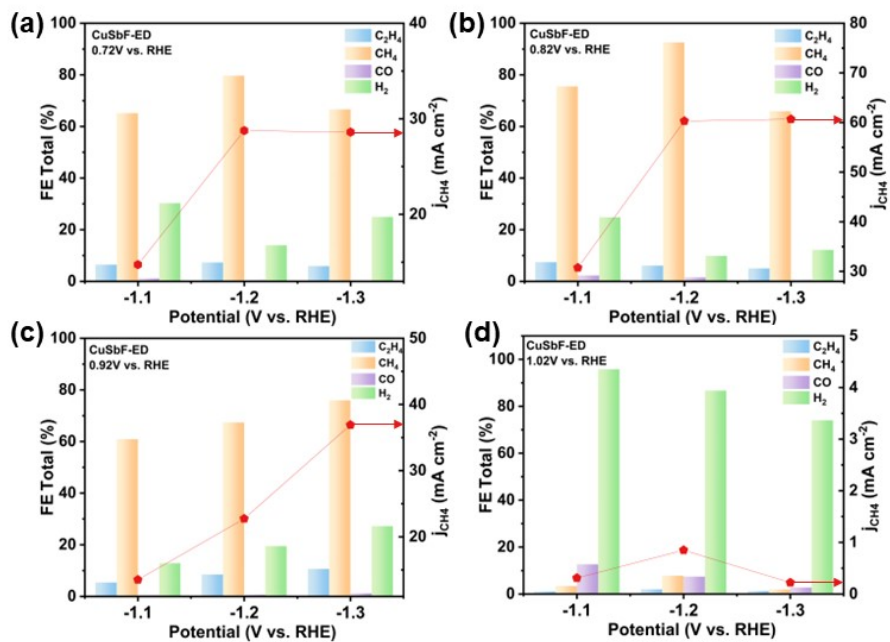


**Fig. S20.** The FE<sub>total</sub> of (a) CuSbF-ED-0.72V, (b) CuSbF-ED-0.82V, (c) CuSbF-ED-0.92V, (d) CuSbF-ED-1.02V, and (e) 1M CuSbF-ED in CO<sub>2</sub>-saturated 0.5 M KHCO<sub>3</sub> solution.

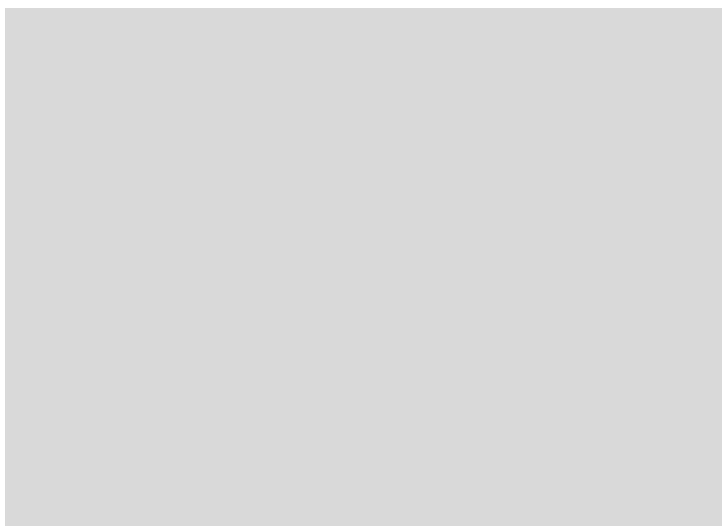


**Fig. S21.**  $FE_{CH_4}$  and  $j_{CH_4}$  of CuSbF-ED in different electrolytes.

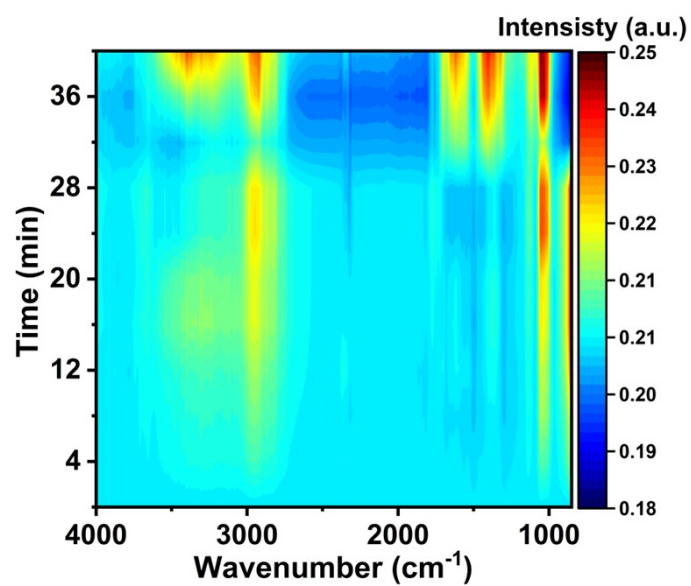


**Fig. S22.** Contour plots of in situ ATR-FTIR spectra of CuSbF-ED collected at -1.2 V vs RHE in CO<sub>2</sub>-saturated 0.5 M KHCO<sub>3</sub> electrolyte.

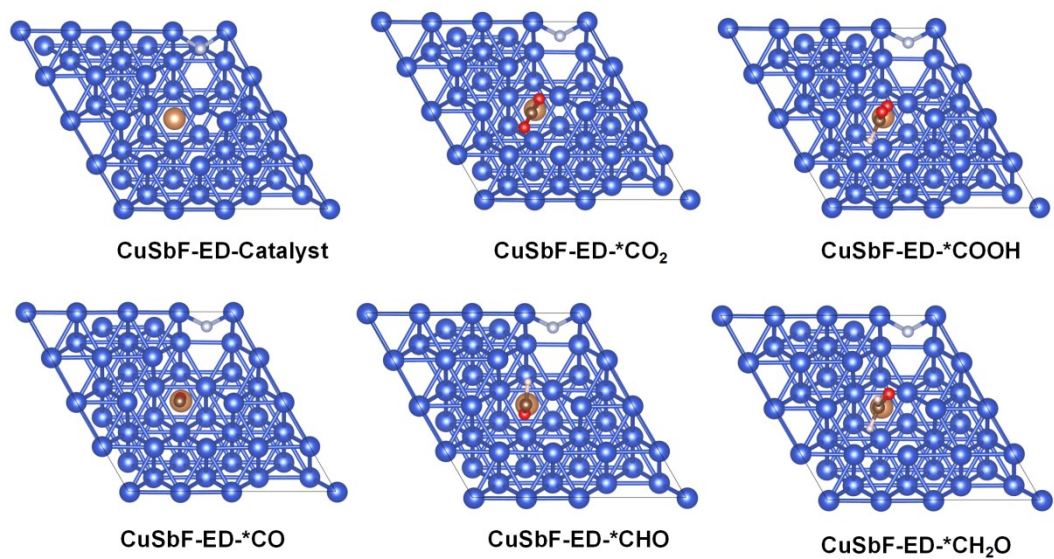


**Fig. S23.** The adsorption configurations of \*CO<sub>2</sub>, \*COOH, \*CO, \*CHO, and \*CH<sub>2</sub>O on CuSbF-ED.

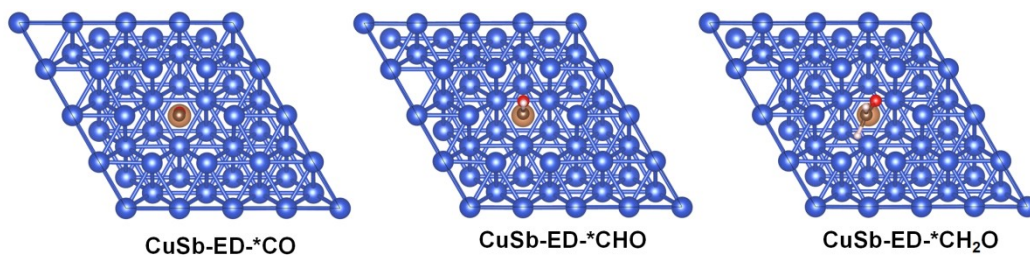


**Fig. S24.** The adsorption configurations of \*CO, \*CHO, and \*CH<sub>2</sub>O on CuSb-ED.

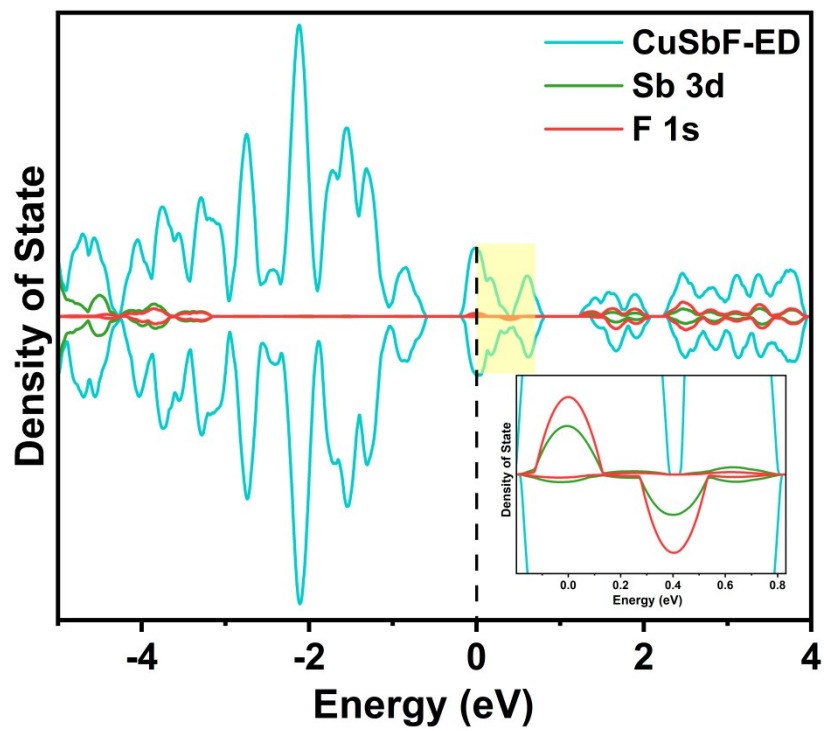
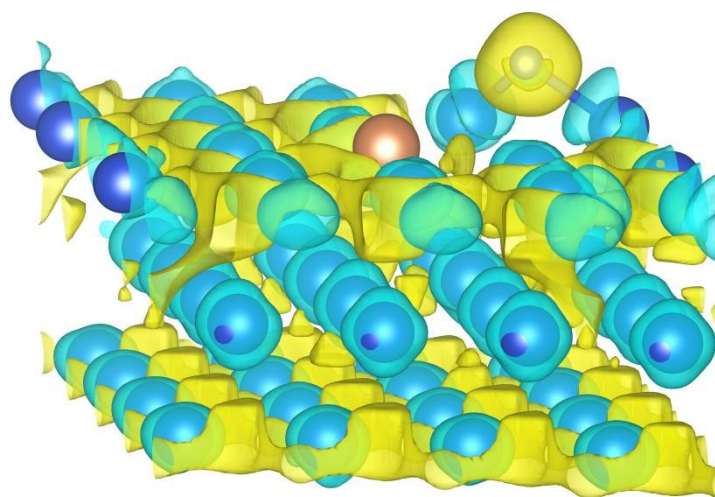


Fig. S25. The calculated density of states of Sb and F orbitals for CuSbF-ED.



**Fig. S26.** Charge density difference of the CuSbF-ED model. The yellow and green areas represent the electron accumulation and depletion, respectively.

**Table S1.** XPS atomic quantitative analysis of CuSbF-ED, CuSb-ED, and CuF-ED.

<b>Catalysts</b>	<b>Species atomic %</b>		
	<b>Cu</b>	<b>Sb</b>	<b>F</b>
CuSbF-ED	37.9	2.89	8.80
CuSb-ED	36.13	2.55	–
CuF-ED	32.81	–	1.83

**Table S2.**  $FE_{CH_4}$  Comparison for various Cu-based catalysts.

Catalysts	Electrolyte	$FE_{CH_4}$ (%)	Partial Current Density of $CH_4$ ( $mA\ cm^{-2}$ )	Ref.
HATNA-Cu-MOF	0.1 M $KHCO_3$	78	8.2	(10)
$Cu_2O@Cu$ -HHTP	0.1 M $KHCO_3$	73	10.8	(11)
$Cu_4$ -MFU-4l	0.5 M $NaHCO_3$	92	9.8	(12)
Cu-I MOFs	1 M KOH	57.2	60.7	(13)
CuPc	0.5 M $KHCO_3$	66	13.2	(14)
$Cu_3(PO_4)_2$ (x8)	0.1 M $KHCO_3$	76	15.2	(15)
$Cu_3(DMP_z)_3$	0.1M KCL	80	8	(16)
Cu-P-ED	0.5 M $NaHCO_3$	85	38	(17)
CuSbF-ED	0.5 M $KHCO_3$	92.6	60.3	This work

**Table S3.** Tafel slope, intercept and relative activation energy of Cu Foil, CuSb-ED, CuF-ED, and CuSbF-ED catalysts.

<b>Catalyst</b>	<b>Tafel slope</b>	<b>Intercept</b>	<b><math>j_0</math> (mA·cm<sup>-2</sup>)</b>	<b>Relative activation energy<sup>a</sup></b>
Cu Foil	-1.01	-0.33	0.46	1.66
CuSb-ED	-0.42	-0.23	0.59	1.13
CuF-ED	-0.60	-0.26	0.55	1.28
CuSbF-ED	-0.21	-0.20	0.63	1

<sup>a</sup>Activation energy relative to CuSbF-ED.

**Table S4.** Change of Gibbs free energy for CH<sub>4</sub> production pathway over CuSbF-ED with pulsed potential electrolysis.

<b>Reaction pathway</b>	<b>Change of Gibbs free energy (eV)</b>
CuSbF-ED + CO <sub>2</sub> → *CO <sub>2</sub>	0.40
*CO <sub>2</sub> + H → *COOH	0.83
*COOH + H → *CO + H <sub>2</sub> O	-0.99
*CO + H → *CHO	1.39
*CHO + H → *CH <sub>2</sub> O	-2.02

**Table S5.** Change of Gibbs free energy for CH<sub>4</sub> production pathway on Cu(111) of CuSb-ED with pulsed potential electrolysis.

<b>Reaction pathway</b>	<b>Change of Gibbs free energy (eV)</b>
*CO + H → *CHO	1.41
*CHO + H → *CH <sub>2</sub> O	-2.15

## References

1. J. Huang, M. Mensi, E. Oveisi, V. Mantella and R. Buonsanti, *Journal of the American Chemical Society*, 2019, 141, 2490-2499.
2. G. Kresse and J. Hafner, *Physical Review B*, 1994, 49, 14251-14269.
3. G. Kresse and J. Furthmüller, *Physical Review B*, 1996, 54, 11169-11186.
4. P. E. Blöchl, *Physical Review B*, 1994, 50, 17953-17979.
5. J. P. Perdew, K. Burke and M. Ernzerhof, *Physical Review Letters*, 1996, 77, 3865-3868.
6. R. P. White and J. E. G. Lipson, *Macromolecules*, 2018, 51, 4896-4909.
7. E. R. Homer, O. K. Johnson, D. Britton, J. E. Patterson, E. T. Sevy and G. B. Thompson, *npj Computational Materials*, 2022, 8, 157.
8. M. Jawad, A. H. Majeed, K. S. Nisar, M. B. Ben Hamida, A. Alasiri, A. M. Hassan, H. Shahzad, S. M. Eldin and S. W. Sharshir, *Case Studies in Thermal Engineering*, 2023, 50, 103413.
9. I. W. M. Smith, *Chemical Society Reviews*, 2008, 37, 812-826.
10. Y. Liu, S. Li, L. Dai, J. Li, J. Lv, Z. Zhu, A. Yin, P. Li and B. Wang, *Angewandte Chemie International Edition*, 2021, 60, 16409-16415.
11. J.-D. Yi, R. Xie, Z.-L. Xie, G.-L. Chai, T.-F. Liu, R.-P. Chen, Y.-B. Huang and R. Cao, *Angewandte Chemie International Edition*, 2020, 59, 23641-23648.
12. H.-L. Zhu, J.-R. Huang, X.-W. Zhang, C. Wang, N.-Y. Huang, P.-Q. Liao and X.-M. Chen, *ACS Catalysis*, 2021, 11, 11786-11792.
13. Y. Zhang, Q. Zhou, Z.-F. Qiu, X.-Y. Zhang, J.-Q. Chen, Y. Zhao, F. Gong and W.-Y. Sun, *Advanced Functional Materials*, 2022, 32, 2203677.
14. Z. Weng, Y. Wu, M. Wang, J. Jiang, K. Yang, S. Huo, X.-F. Wang, Q. Ma, G. W. Brudvig, V. S. Batista, Y. Liang, Z. Feng and H. Wang, *Nature Communications*, 2018, 9, 415.
15. B. Zhang, J. Zhang, P. An, Z. Su, Q. Wan, X. Tan and L. Zheng, *Nano Energy*, 2021, 88, 106239.
16. X.-D. Zhang, T. Liu, C. Liu, D.-S. Zheng, J.-M. Huang, Q.-W. Liu, W.-W. Yuan, Y. Yin, L.-R. Huang, M. Xu, Y. Li and Z.-Y. Gu, *Journal of the American Chemical Society*, 2023, 145, 2195-2206.
17. Y.-L. Qiu, H.-X. Zhong, T.-T. Zhang, W.-B. Xu, X.-F. Li and H.-M. Zhang, *ACS Catalysis*, 2017, 7, 6302-6310.